Submitted to

31st International Conference on High Energy Physics, ICHEP02, July 24, 2002, Amsterdam
Abstract: **1019**
Parallel Session **4,10**

www-h1.desy.de/h1/www/publications/conf/conf_list.html

Multi-electron Production at High Transverse Momentum in ep collisions at HERA

H1 Collaboration

Abstract

Multi-electron production has been measured at high transverse momentum in 115 pb^{-1} of positron- and electron-proton collisions collected by the H1 experiment at HERA. Good overall agreement is found with the Standard Model predictions, dominated by photon-photon interactions. Six events are observed with a di-electron mass above 100 GeV, a domain where the Standard Model prediction is low.

1 Introduction

The measurement of rare processes in electron[1]-proton interactions at HERA provides a unique method to search for new physics. In this paper we report on the first measurement of multi-electron production performed at high transverse momentum (P_T) at HERA. Within the Standard Model (SM) the production of multilepton events in ep collisions is possible mainly through photon-photon interactions, where quasi-real photons radiated from the incident electron and proton interact for producing a pair of leptons $\gamma\gamma \to \ell^+\ell^-$ [1]. An excess of events in a given kinematic domain compared to the SM might be a signature for new phenomena.

The analysis is based on the $e^{\pm}p$ collisions recorded by the H1 experiment in the 1994-2000 period. The total integrated luminosity of 115.2 pb^{-1} is shared between 36.5 pb^{-1} and 65.1 pb^{-1} of e^+p collisions recorded at center of mass energies $\sqrt{s}$ of 300 GeV and 318 GeV respectively, and 13.6 pb^{-1} of e^-p collisions recorded at $\sqrt{s}$ = 318 GeV.

2 Experimental conditions

A detailed description of the H1 detector can be found in [2]. Only components essential for this analysis are shortly described here[2].

A tracking system of central and forward drift chambers is used to measure the charged particle trajectories and to determine the interaction vertex. Particle transverse momenta are determined from the curvature of the trajectories in a magnetic field of 1.15 Tesla.

Hadronic and electromagnetic final state particles are absorbed in a highly segmented liquid argon calorimeter [3] covering the polar angular range $4^\circ < \theta < 153^\circ$. The calorimeter is 5 to 8 hadronic interaction lengths deep depending on the polar angle of the particle. It includes an electromagnetic section which is 20 to 30 radiation lengths deep. Electromagnetic shower energies are measured with a precision of $\sigma(E)/E = 12\%/\sqrt{E/\mathrm{GeV}} \oplus 1\%$ and hadronic shower energies with $\sigma(E)/E = 50\%/\sqrt{E/\mathrm{GeV}} \oplus 2\%$ as measured in test beams [4]. The electromagnetic energy scale is known to the level of 0.7 to 3% depending on the polar angle. The hadronic energy scale is understood at the 2% level.

In the backward region the liquid argon calorimeter is completed by a lead/scintillating-fibre calorimeter [3][5] covering the range $155^\circ < \theta < 178^\circ$, and by electron and photon taggers located downstream of the interaction point in the electron beam direction. The calorimeter is surrounded by a superconducting coil and an iron yoke instrumented with streamer tubes. Leakage of hadronic showers outside the calorimeter is measured from an analogue charge sampling of the streamer tubes (Tail Catcher).

The analysis is restricted to periods where the central drift chambers, the liquid argon calorimeter and the luminosity system are active and fully operational. For the analysed topologies trigger conditions are derived from the liquid argon calorimeter signals. The trigger efficiency is higher than 95% for events with an electron energy above 10 GeV.

[1] In this paper the term "electron" is used to describe generically electrons or positrons.

[2] The origin of the H1 coordinate system is the nominal ep interaction point. The direction of the incoming proton defines the z-axis for the measurement of polar and azimuthal angles as well as for transverse momenta. It also defines the forward region of the detector.

[3] This device was installed in 1995 replacing a lead-scintillator "sandwich" calorimeter [2].

3 Standard Model Processes and their Simulation

The main SM processes involved in multi-electron production at HERA are summarized in figure 1. The dominant contribution is the interaction of two photons radiated from the incident electron and proton, either in the elastic or quasi-elastic mode (figure 1a), or in the inelastic mode (figure 1b). The Cabibbo-Parisi process (figure 1c), which can also be elastic or inelastic, involves an e^+e^- interaction where one of the electrons is issued from a photon radiated from the proton. Its contribution is one order of magnitude lower, except at high transverse momentum where it contributes more significantly. The Drell-Yan process (figure 1d) involves a quark-antiquark interaction where one of the quarks is issued from a photon radiated from the incident electron. Its contribution is negligible in the entire measured phase space [6].

Multi-lepton event production is simulated with the GRAPE Monte Carlo generator [7]. GRAPE is based on the symbolic graphs calculation system GRACE [8]. It simulates the full $2 \to 4$ electroweak matrix elements at tree level, except for the negligible Drell-Yan contribution, for interactions resulting in three leptons plus hadrons in the final state. GRAPE contains $\gamma\gamma$ graphs with interference effects between the scattered and produced electrons. It takes into account the Cabibbo-Parisi process, photon internal conversions (diagrams containing a radiated photon with subsequent $\gamma \to e^+e^-$ vertex) and Z^0 production or virtual exchange. Initial and final state radiation processes (QED and QCD - parton showers) are simulated in the leading log approximation. The proton dissociation is treated in three phase space regions: elastic, quasielastic and inelastic. In order to simulate experimental distributions the GRAPE generator was interfaced to the H1 detector simulation.

GRAPE was cross-checked with the generator LPAIR [9], which contains only the photon-photon process generated in the Weizsäcker-Williams approximation without interference terms or weak contributions. When restricted to the same processes, GRAPE agrees with LPAIR at the percent level for both total and differential cross-sections. The additional diagrams in GRAPE increase the predicted cross-section by 20 % in average, and up to 40 % for di-lepton masses either very low (photon internal conversions) or around 90 GeV (Z^0 production). At masses higher than the Z^0 mass, the difference between GRAPE and LPAIR is dominated by the weak interference, which has a 10% negative effect for the dominant e^+p sample.

The main experimental backgrounds to multi-electron production are processes where, in addition to a true electron, one or more fake electrons may be reconstructed from the final state particles. The dominant contribution is expected from Neutral Current Deep Inelastic Scattering (NC-DIS) where a fake electron from the hadrons or some radiated photon is selected together with the scattered electron. Elastic Compton scattering can also contribute if the high P_T photon is misidentified as an electron. The NC-DIS and elastic Compton processes are simulated with the DJANGO [10] and WABGEN [11] generators respectively.

The Monte-Carlo predictions are attributed theoretical and experimental systematic uncertainties added in quadrature. The theoretical errors reflect the available freedom in the proton parton distributions and in the choice of internal cuts between different phase space regions used in the generators. The main experimental uncertainty is due to the tracker efficiency in the electron identification procedure (see below). Uncertainties on the energy scales of the calorimeters, the trigger efficiency and the luminosity measurement are also taken into account. The prediction of fake electron background contributions has been studied in control analyses described in the next section and the corresponding systematical error is taken into account.

4 Event Selection

The multi-electron event selection is based on an electron identification procedure designed to minimize the contribution of fake electrons, while keeping a high efficiency for true electrons and a reliable control of the overall selection performance.

Electrons with energies above 5 GeV are first preselected in the fiducial volume of the liquid argon and SPACAL calorimeters, covering the polar angular range $5^\circ < \theta < 175^\circ$. Isolated electromagnetic showers are sorted out using pattern recognition algorithms based on the geometric profiles expected from electrons. The remaining clusters - related to hadronic activity - are combined into hadronic jets using a k_T algorithm [12]. In the region of overlap between the liquid argon calorimeter and the central drift chamber ($20^\circ < \theta < 150^\circ$), the calorimetric identification is complemented by a tight tracking condition, requiring that an isolated high quality track matches the electromagnetic cluster both geometrically and in momentum. This additional constraint strongly reduces the contribution of fake electrons issued from photons and hadrons. Electrons selected in this polar angular range are called "central electrons" hereafter. In the forward ($5^\circ < \theta < 20^\circ$) and backward ($150^\circ < \theta < 175^\circ$) regions no explicit track requirement is made. The forward electron energy threshold is raised to 10 GeV in order to minimize the contribution of NC-DIS forward jets to fake electrons. Once identified, only electron candidates isolated from each other and from hadronic jets by more than 0.5 radians in the pseudorapidity-azimuth plane are considered.

The performance and reliability of this harsh electron identification procedure was controlled in several ways. The tracking efficiency was measured with a NC-DIS sample selected with no tracking conditions for the electron candidate, requiring a single electromagnetic cluster in the calorimeter with a transverse momentum above 10 GeV in the polar angle interval $20^\circ < \theta < 150^\circ$. Figure 2 shows that the average efficiency is 90 % and varies only slightly with the track momentum and polar angle. The decrease observed in the forward region is due to the electron showering. The measured efficiency is described by the simulation with an accuracy ranging from 3 % in the central region to 15 % at the edge of the angular acceptance of the central tracker. Electron misidentification was studied by measuring the probability to select a second electron in NC-DIS events when relaxing the track quality criteria. In case no tracking conditions are applied to the second electromagnetic cluster, fake electrons are dominated by photons of elastic Compton events (figure 3 left). This contribution is drastically reduced by a loose tracking requirement (figure 3 right). In both cases fake electron background is described by the simulation to within 20 %. Photon conversions were investigated using a sample enriched with elastic Compton events, selected by requiring one central electron plus a second electromagnetic cluster (photon candidate) and no significant extra energy in the calorimeters. The charged tracks associated to the photon candidate are studied in figure 4. Their number (figure 4 left) and starting radius in the transverse plane (figure 4 right) are well reproduced by the simulation. On figure 4 right, the central tracker structure is visible as peaks in the distribution, corresponding to the photon conversions in the tracker walls. These conversions are well described.

The selection of the multi-electron events requires two central electron candidates, out of which one must have $P_T > 10$ GeV and the second one $P_T > 5$ GeV. Additional electron candidates are identified in the forward, central or backward regions with no explicit P_T cut. The electron candidates are indexed in decreasing P_T: $P_T^{e_i} > P_T^{e_{i+1}}$.

The selected events are classified as di-electrons ("2e") in the case where only the two central electron candidates are visible, and tri-electrons ("3e") in the case where exactly one additional electron candidate is identified. No event is observed with more that one additional electron. In addition, a subsample of the "2e" sample, labelled "$\gamma\gamma$", is selected in order to measure the photon-photon cross section in a well defined phase space with low background. In this subsample, the two electrons must be of opposite charge, and a significant deficit compared to the initial state must be observed in the difference $E - P_z$ of the energy and longitudinal momentum of all visible particles ($E - P_z < 45$ GeV) [4]. These two conditions ensure that the incident electron is lost in the beam pipe after radiating a quasi-real photon of squared momentum Q^2 lower than 1 GeV^2.

5 Results

The event yields for each sample are summarized in table 1. The observed numbers of di-electron and tri-electron events are in agreement with the expectations. No event is seen with four or more identified electrons.

The distributions of the global event variables are presented in figure 5. The 3e events accumulate at $E - P_z$ values around 55 GeV, as expected since the scattered electron is visible in the detector. The 2e events show a tail at lower $E - P_z$, due to the incident electron being lost in the beam pipe, corresponding to the $\gamma\gamma$ topology described above. The transverse momentum is balanced within resolution as quantified by the vectorial sum P_T^{miss} of the transverse momenta of all visible particles. The P_T^{miss} distribution is consistent with the expectation for no emission of undetected particles with substantial transverse momentum. The inelasticity spectrum, as measured from the transverse momentum $P_T^{hadrons}$ of all visible particles except identified electrons, is also well described by the SM.

The distributions of the individual electron transverse momenta $P_T^{e_i}$ are steeply falling as shown in figure 6. The 2e and 3e samples are in good overall agreement with the SM. Three 2e events are seen with $P_T^{e_1}$ above 50 GeV, a domain where the SM expectation is low. The electron polar angle θ^{e_i} distributions are rather uniform (figure 7) and in agreement with the SM.

The distribution of the invariant mass M_{12} of the two highest P_T electrons in the event, and its correlation with respect to $P_T^{e_1} + P_T^{e_2}$, are shown in figure 8. Three 2e and three 3e events are seen with invariant masses M_{12} above 100 GeV, where the SM expectation is low. The three 2e events are the same as those observed at high P_T^{e1}. The comparison to the SM expectations of the observed event rates for masses above 100 GeV is presented in table 2. The invariant masses of the other possible electron combinations in the 3e sample are shown in figure 9. No event is seen with an unexpected high M_{13} or M_{23}. The three high M_{12} events have also a high tri-electron mass M_{123}.

[4]For events where only longitudinal momentum along the proton direction is undetected, one expects $E - P_z = 2E_e = 55$ GeV, where E_e is the energy of the incident electron. The threshold $E - P_z < 45$ GeV corresponds to a cut on the fractional energy loss $y = \frac{E-P_z}{2E_e^0} < 0.82$.

The six events with $M_{12} > 100$ GeV were recorded in the positron-proton collisions. They are shown individually in figures 10 to 15 . For these events, all available detector signals support the interpretation of the electron candidates as being electrons. The electromagnetic shower shapes were checked individually to be as expected from the calorimeter response to electrons. All central tracks yield a specific ionization in the central drift chamber as expected from single electrons. The forward electron candidates in events 4, 5 and 6 all have at least one track pointing to the calorimetric energy cluster, though no such requirement was set in their identification. The measurements of the central electron momenta by the tracker and the calorimeter are compatible with each other within errors.

Though classified as 2e, event 1 also contains a third electron candidate with energy below the identification threshold. Similarly event 3 has a compact electromagnetic energy deposit located at the forward boundary of the liquid argon calorimeter, outside the electron identification fiducial volume. This event also shows a low energy converted photon radiated close to electron e_2. With the exception of event 6, which has a significant forward hadronic jet, the events show no hadronic activity in the detector. It should be noted that the high mass electron pair topology differs for events classified as "2e" and "3e": in the former case, the high-mass pair is formed of two central high-P_T electrons, whereas in the latter case, it contains one forward and one central electron of intermediate P_T's (figure 8).

The photon-photon differential cross-sections measured with the $\gamma\gamma$ sample as function of $P_T^{hadrons}$, $P_T^{e_1}$ and M_{12} are shown in figures 16, 17 and 18 respectively. These cross sections are extracted in the restricted kinematical domain defined by $20^\circ < \theta^{e_{1,2}} < 150^\circ$, $P_T^{e_1} > 10$ GeV, $P_T^{e_2} > 5$ GeV, incident electron fractional energy loss $y < 0.82$, and $Q^2 < 1$ GeV^2. A good agreement with the SM is found for all three variables [5].

6 Summary

High-P_T multi-electron production has been measured for the first time in ep scattering at HERA. No event was found with four or more identified electrons. The di-electron and tri-electron event yields are in good overall agreement with the Standard Model predictions, dominated by photon-photon interactions. The differential cross-sections for the photon-photon process have been extracted in a restricted phase space and found to agree with the predictions.

For masses of the highest P_T electron pair above 100 GeV, three events classified as di-electrons, and three events classified as tri-electrons are seen, compared to SM expectations of 0.25 ± 0.05 and 0.23 ± 0.04 respectively.

Acknowledgements

We are grateful to the HERA machine group whose outstanding efforts have made and continue to make this experiment possible. We thank the engineers and technicians for their work in

[5] It is worth noting that the agreement in $P_T^{hadrons}$ confirms our understanding of the SM expectation for the excess of events with a high P_T lepton and missing transverse momentum P_T^{miss} observed at high $P_T^{hadrons}$ by H1 in a separate analysis [13].

constructing and now maintaining the H1 detector, our funding agencies for financial support, the DESY technical staff for continual assistance, and the DESY directorate for the hospitality which they extend to the non DESY members of the collaboration.

References

[1] J.A.M. Vermaseren, Nucl. Phys. **B229** (1983) 347.

[2] H1 Collaboration, I. Abt et al., Nucl. Instr. and Meth. A386 (1997) 310 and 348.

[3] H1 Calorimeter Group, B. Andrieu et al., Nucl. Instr. and Meth. A336 (1993) 460.

[4] H1 Calorimeter Group, B. Andrieu et al., Nucl. Inst. and Meth. A344 (1994) 492; *idem*, Nucl. Instr. and Meth. A350 (1994) 57; *idem*, Nucl. Instr. and Meth. A336 (1993) 499.

[5] H1 Spacal Group, R.D. Appuhn et al., Nucl. Instr. and Meth. A386 (1997) 397.

[6] N. Artega-Romero, C. Carimalo, P. Kessler, Zeit.f.Phys **C52** (1991) 289.

[7] T. Abe, Comp. Phys. Comm. **136** (2001) 126, http://www.awa.tohoku.ac.jp/∼tabe/grape/.

[8] T. Ishikawa et al., KEK preprint 92-19 (1993).

[9] S. Baranov, O. Dünger, H. Shooshtari, J.A.M. Vermaseren, Proceedings of the workshop Physics at HERA, Vol. 3 Monte-Carlo Generators, Eds. W. Buchmüller, G. Ingelmann (1991).

[10] DJANGO 2.1; G.A. Schuler and H. Spiesberger, Proceedings of the Workshop Physics at HERA, W. Buchmüller and G. Ingelman (Editors), (October 1991, DESY-Hamburg), vol. 3 p. 1419.

[11] A new Generator for Wide Angle Bremsstrahlung: Ch. Berger and P. Kandel, Proc. of the Monte Carlo Generators for HERA Physics Workshop, DESY-PROC-1999-02, p 596.

[12] S. D. Ellis and D. E. Soper, Phys. Rev. D **48** (1993) 3160 [arXiv:hep-ph/9305266].
C. Adloff *et al.* [H1 Collaboration], Nucl. Phys. B **545** (1999) 3 [arXiv:hep-ex/9901010].

[13] H1 Collaboration, C. Adloff et al., Eur. Phys. J. C5 (1998) 575.

H1 Preliminary 115 **pb**$^{-1}$ **Multi-electron Analysis**

Selection	DATA	SM	GRAPE	NC-DIS + Compton
Visible 2e	105	118.2 ± 12.8	93.3 ± 11.5	25.0 ± 5.5
Visible 3e	16	21.6 ± 3.0	21.5 ± 3.0	0.1 ± 0.1
Visible 4e or more	0	0.1 ± 0.0	0.1 ± 0.0	0.0 ± 0.0
$\gamma\gamma \rightarrow e^+e^-$ subsample	41	48.3 ± 6.1	46.4 ± 6.1	1.9 ± 0.9

Table 1: Observed and predicted multi-electron event rates for the samples described in the text. The prediction errors include model uncertainties and experimental systematical errors added in quadrature.

H1 Preliminary 115 **pb**$^{-1}$ **Multi-electron Analysis**

Selection	DATA	SM	GRAPE	NC-DIS + Compton
Visible 2e $M_{12} > 100$ GeV	3	0.25 ± 0.05	0.21 ± 0.04	0.04 ± 0.03
Visible 3e $M_{12} > 100$ GeV	3	0.23 ± 0.04	0.23 ± 0.04	0.00 ± 0.00

Table 2: Observed and predicted multi-electron event rates for masses $M_{12} > 100$ GeV, for the samples described in the text. The prediction errors include model uncertainties and experimental systematical errors added in quadrature.

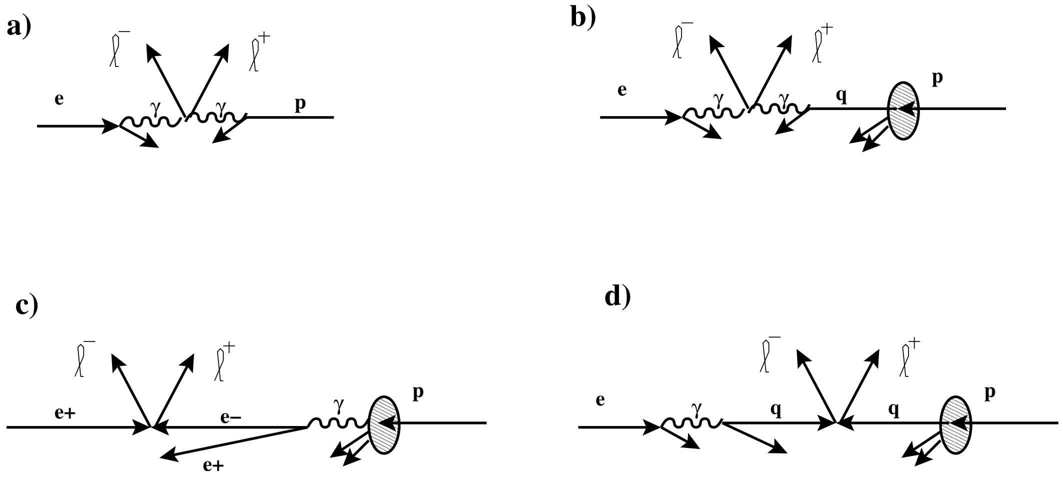

Figure 1: Main processes involved in lepton pair production in ep collisions: a) elastic photon-photon; b) inelastic photon-photon; c) Cabibbo-Parisi; d) Drell-Yan.

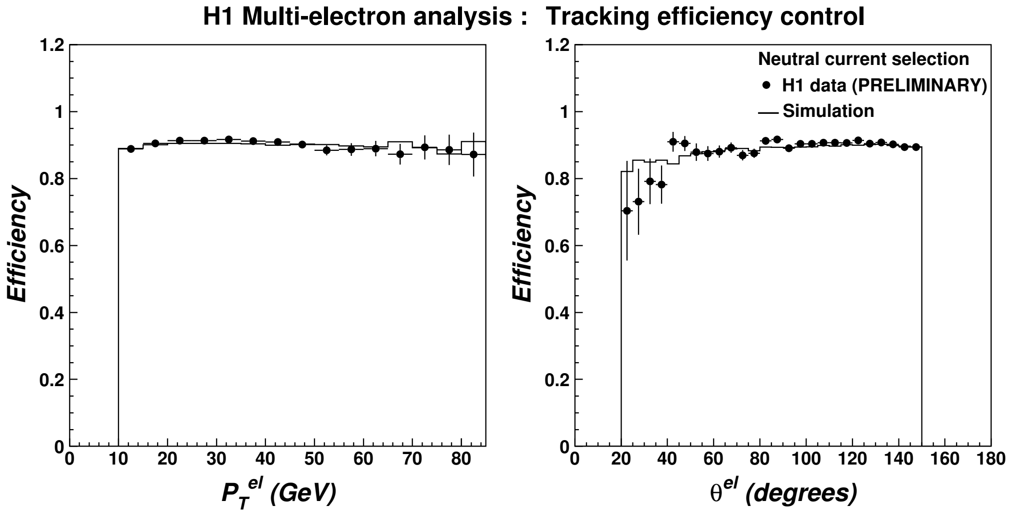

Figure 2: Electron track association efficiency as function of the electron transverse momentum (left) and electron polar angle (right).

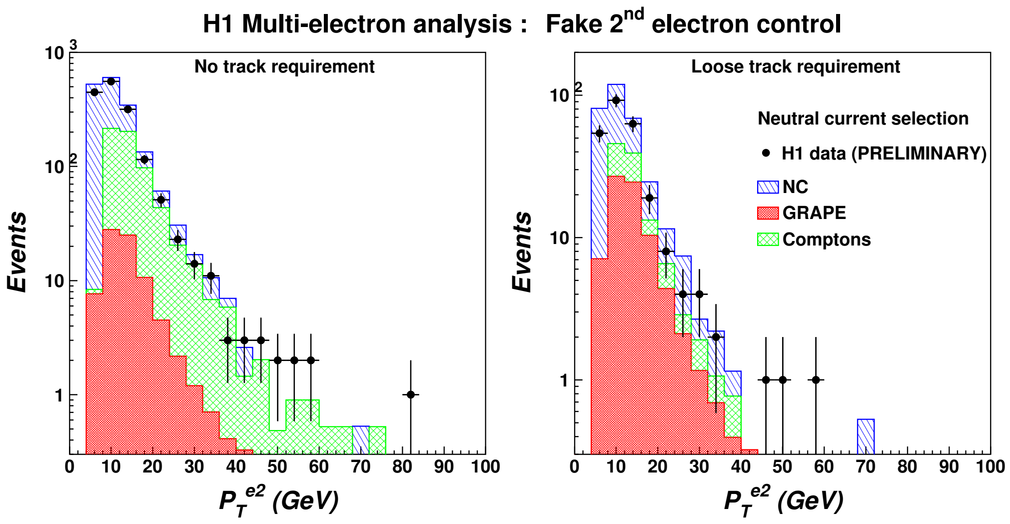

Figure 3: Momentum spectrum of second electrons identified in NC-DIS events with either no track requirement (left) or a loose track requirement (right), compared to expectations.

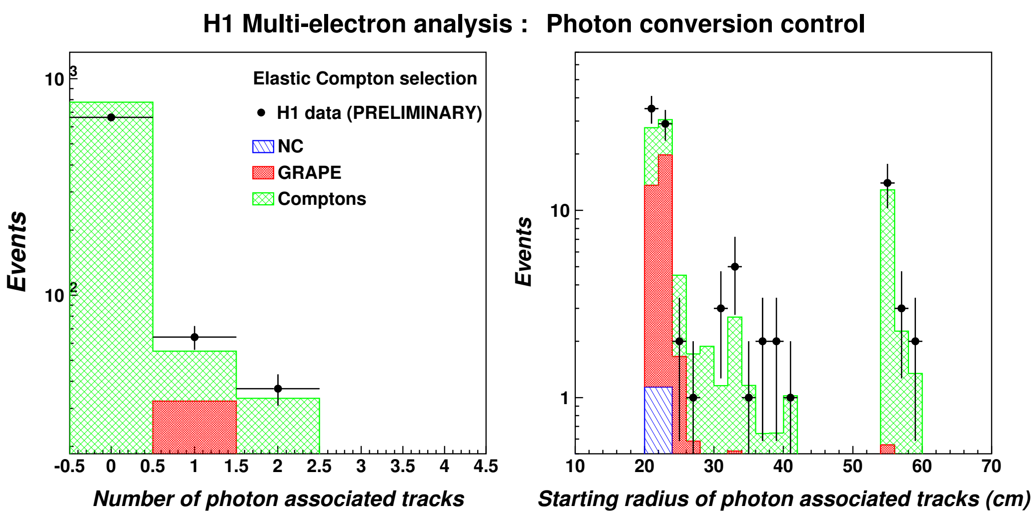

Figure 4: Number (left) and starting radius (right) of the tracks associated to photon candidates in an elastic Compton sample.

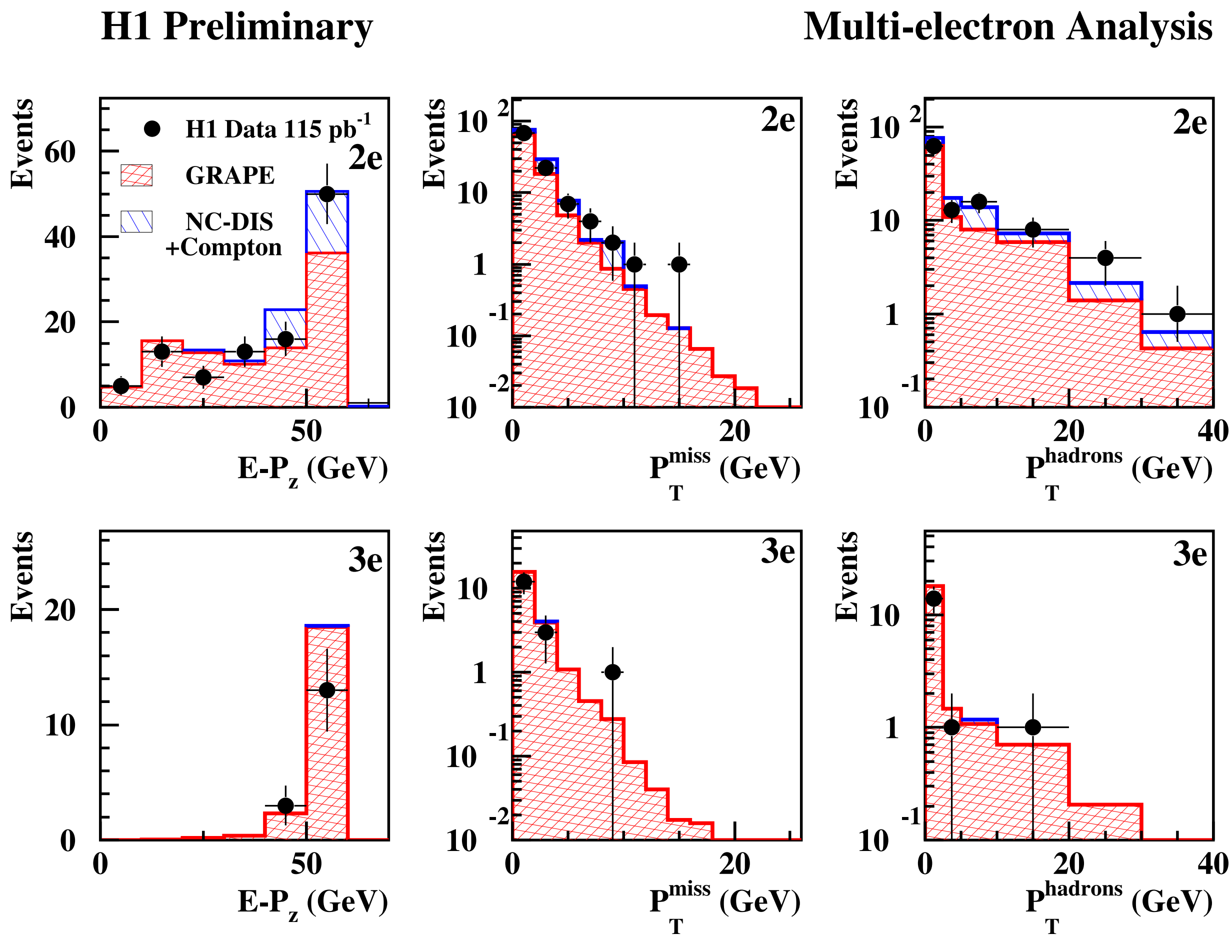

Figure 5: Global event variable distributions (see text) for events classified as di-electrons (top) and tri-electrons (bottom).

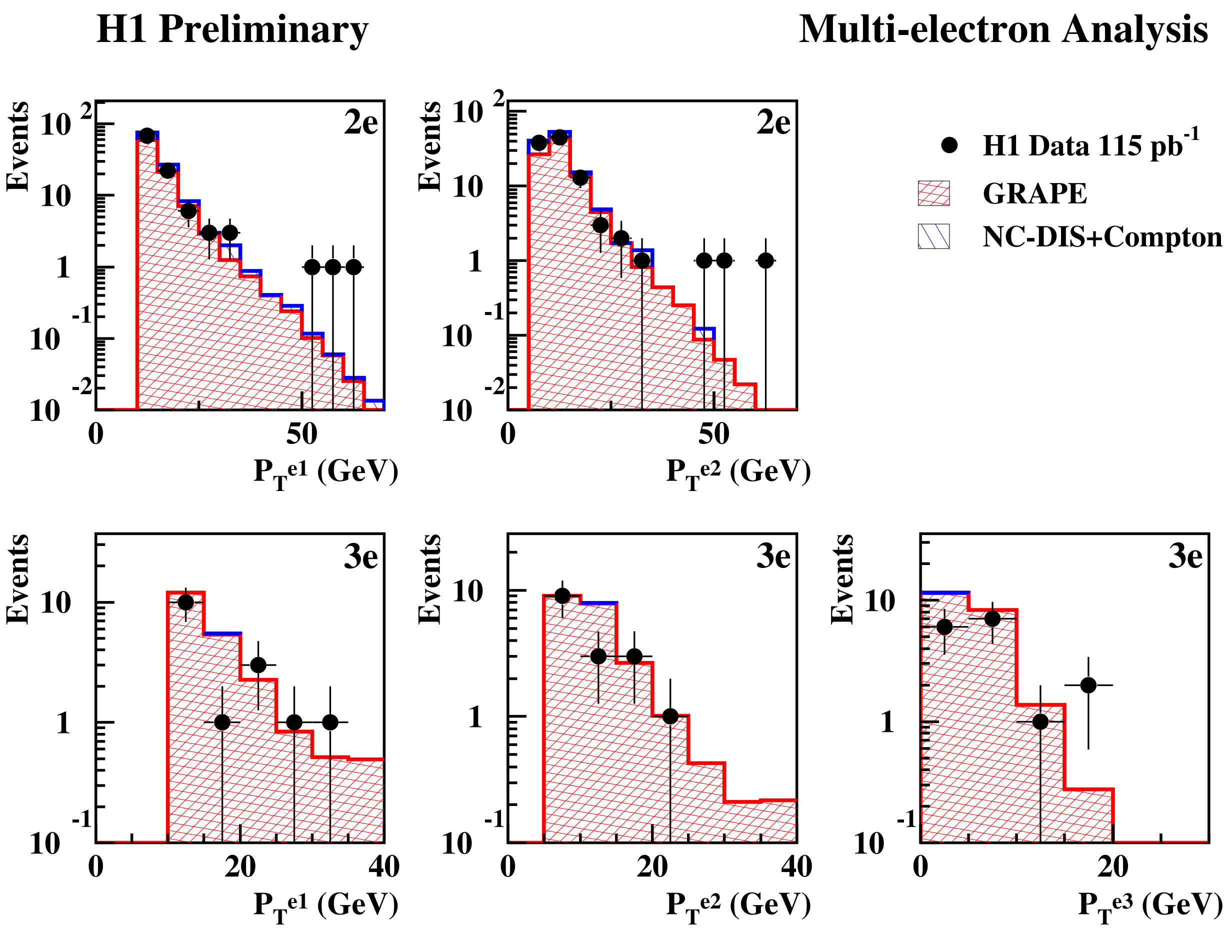

Figure 6: Electron transverse momentum distributions for events classified as di-electrons (top) and tri-electrons (bottom).

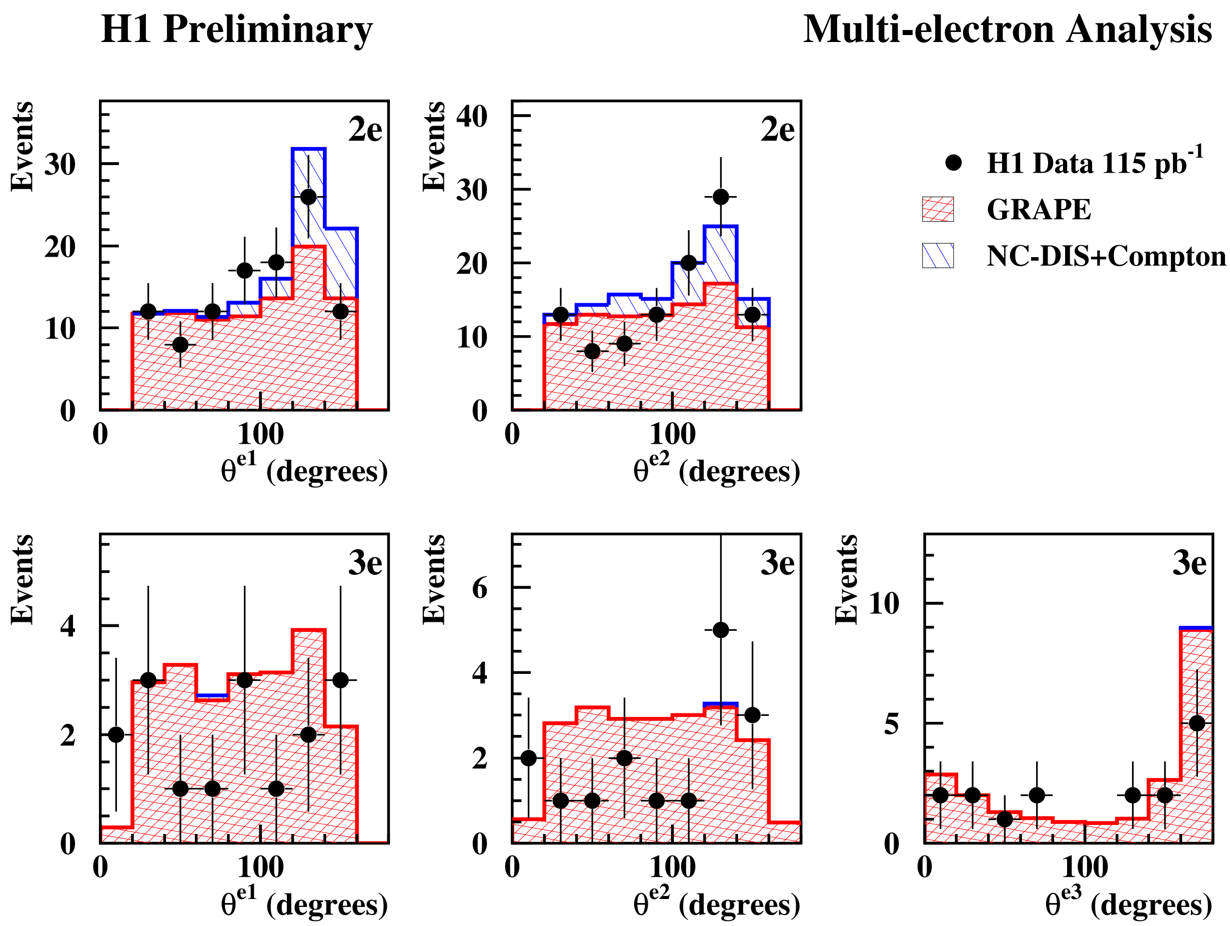

Figure 7: Electron polar angle distributions for events classified as di-electrons (top) and tri-electrons (bottom).

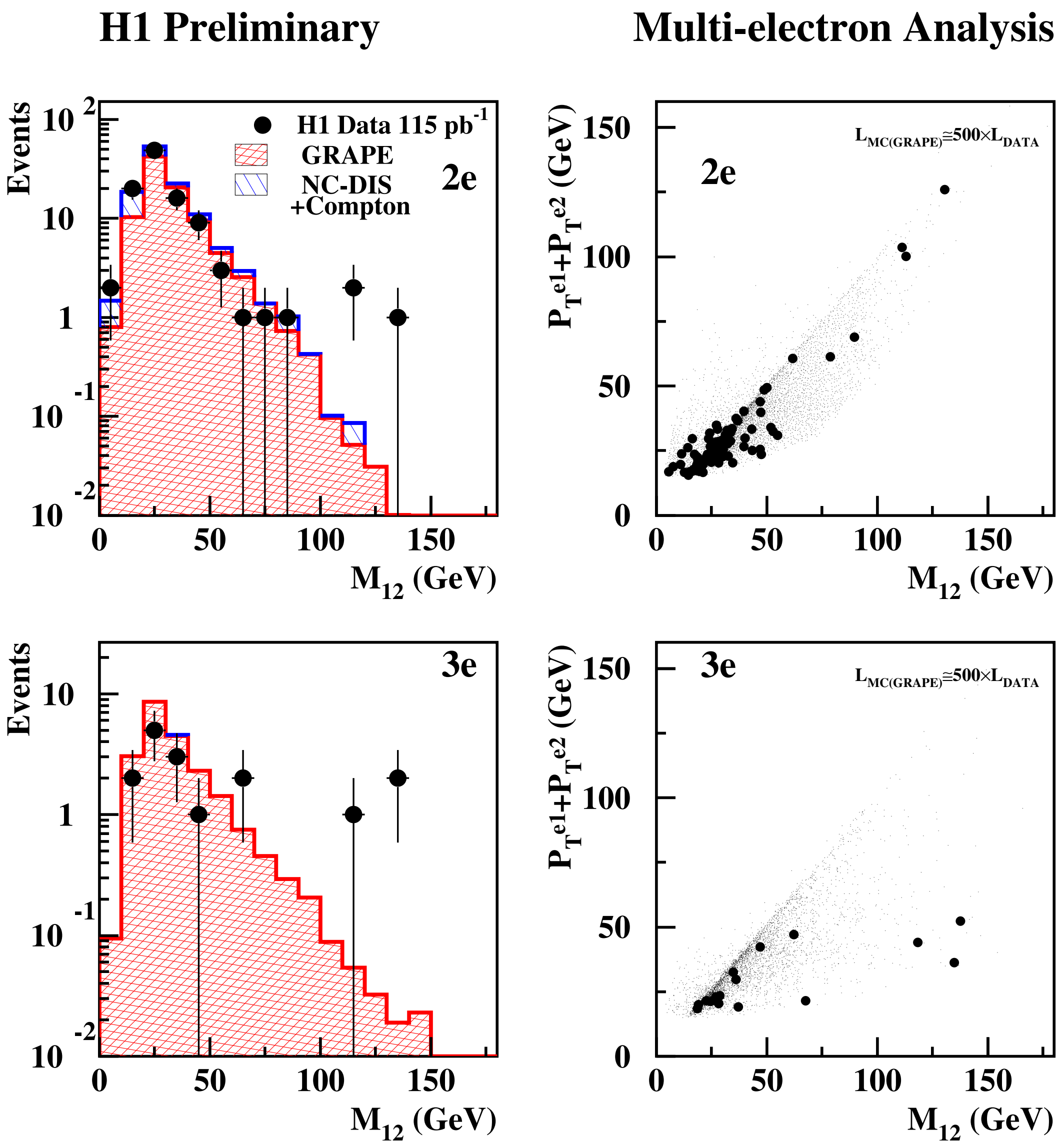

Figure 8: Distribution of the invariant mass M_{12} of the two highest P_T electrons (left) and its correlation with the sum of the electron P_T's (right), for events classified as di-electrons (top) and tri-electrons (bottom). The dots on the right plots represent the Standard Model prediction for a luminosity 500 times higher than in the data.

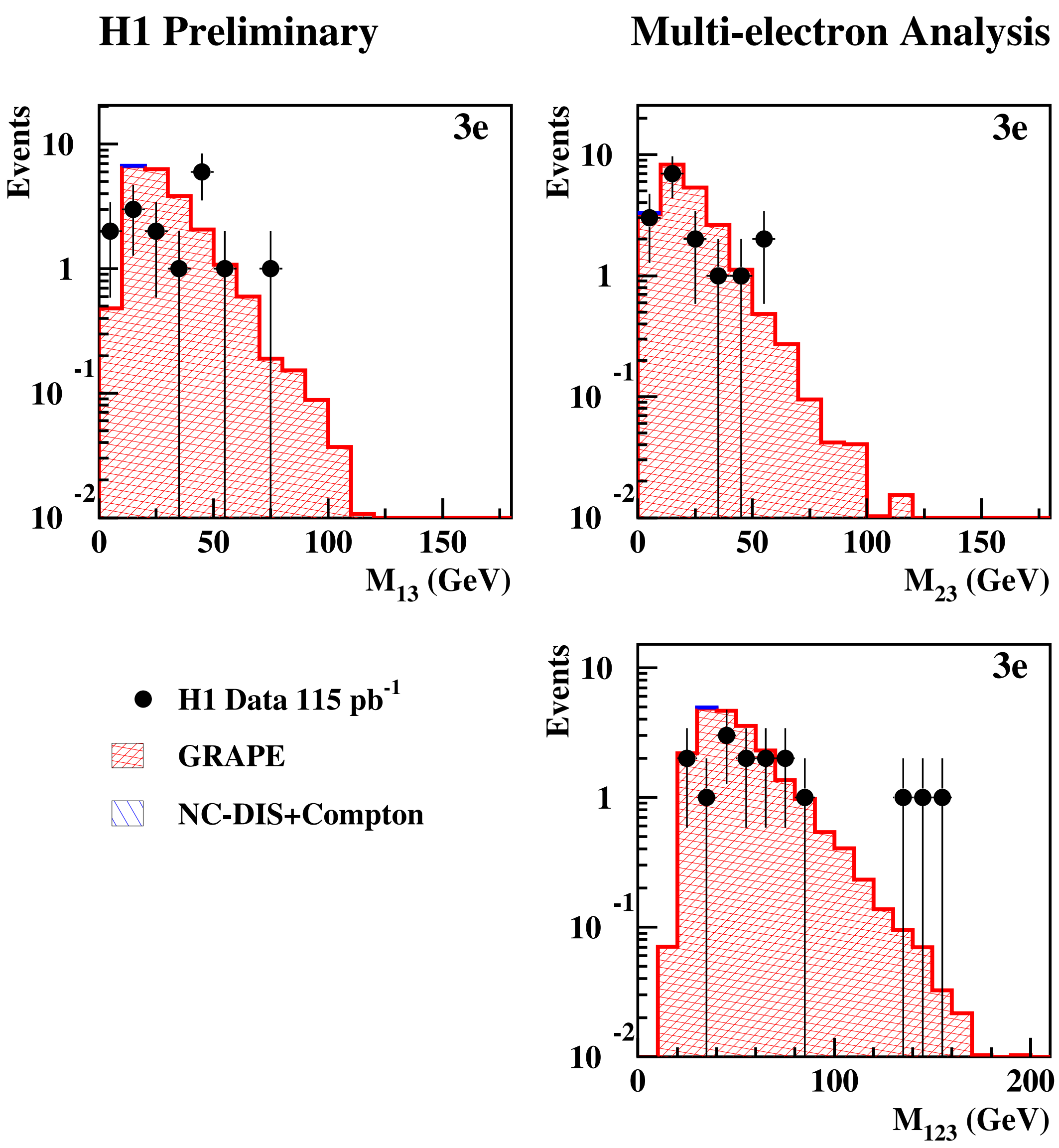

Figure 9: Invariant mass distributions of electron pairs 1-3 and 2-3 (top left and right) and of the tri-electron system (bottom right) for events classified as tri-electrons.

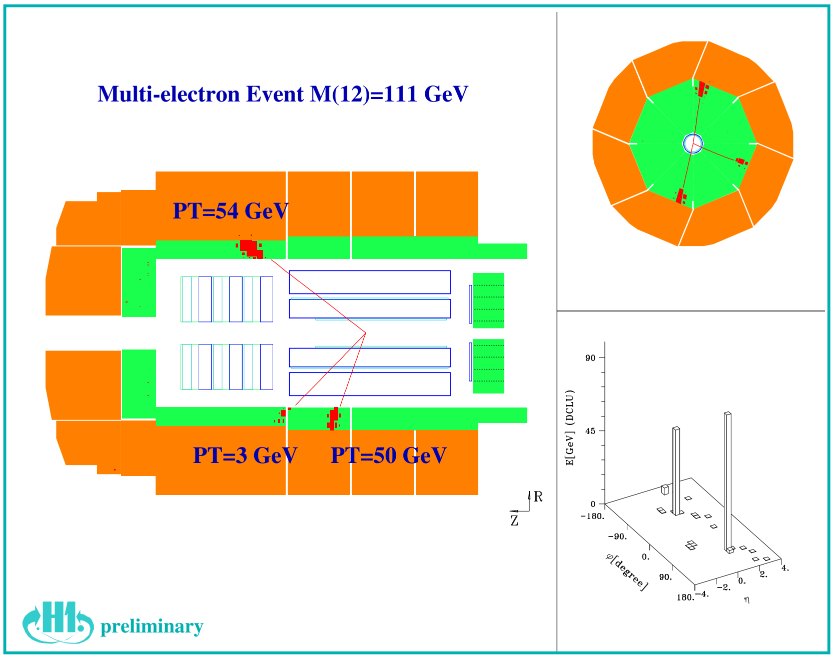

Figure 10: Event Display of **Event 1**, classified as 2e. Indicated are the reconstructed tracks and the energy depositions in the calorimeters. The HERA electrons and protons enter the detector from the left and right, respectively. The third electron candidate visible in this event has an energy lower than the threshold of 5 GeV applied in the electron identification.

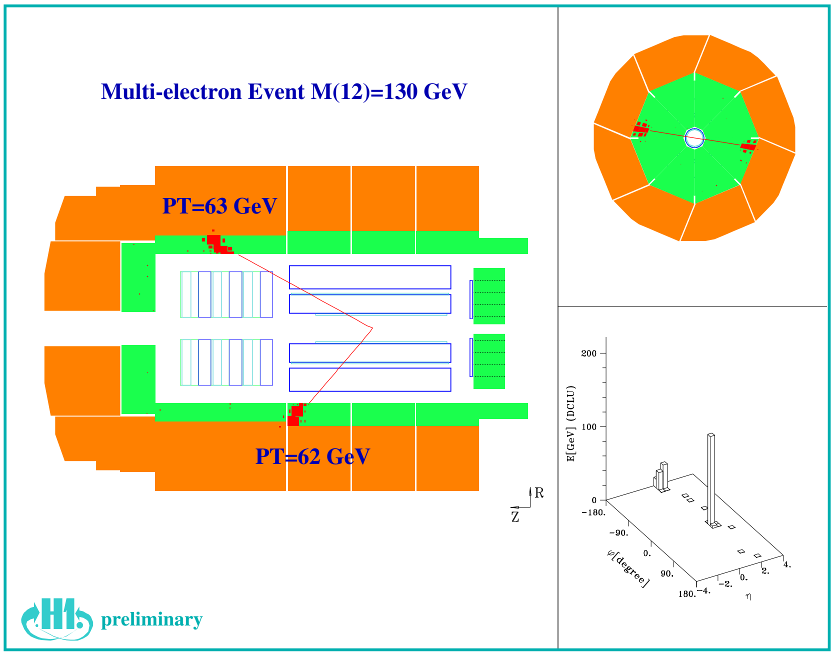

Figure 11: Event Display of **Event 2**, classified as 2e.

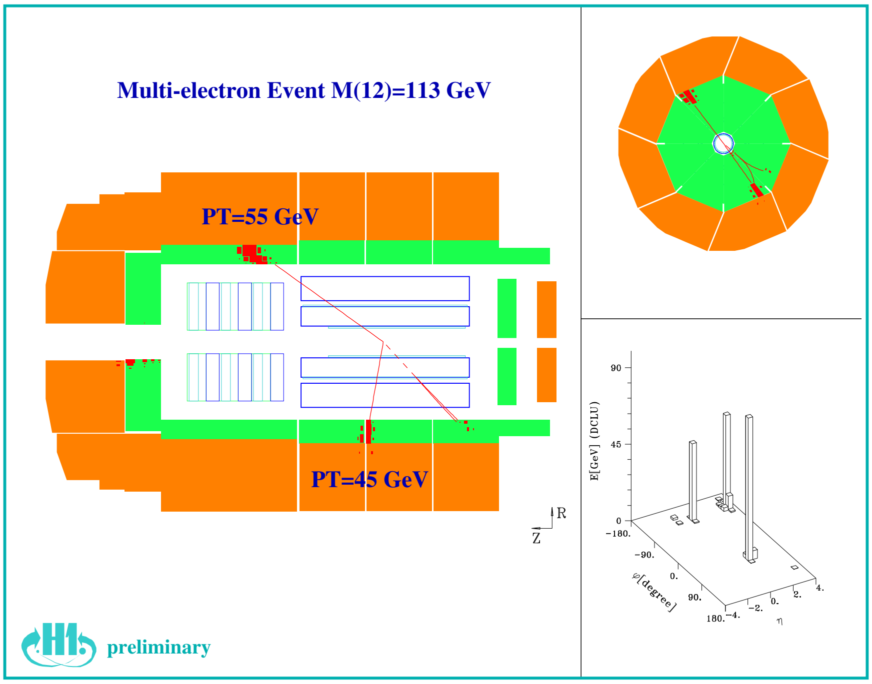

Figure 12: Event Display of **Event 3**, classified as 2e. A third compact electromagnetic energy deposit is located at the forward boundary of the liquid argon calorimeter, outside the electron identification fiducial volume. This event also shows a low energy converted photon in the backward direction close to electron e2.

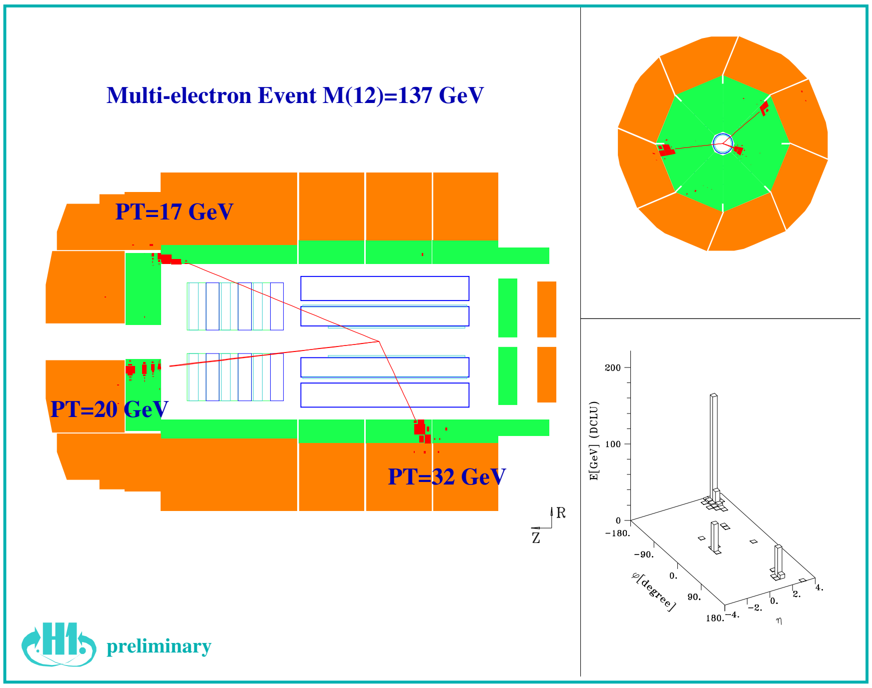

Figure 13: Event Display of **Event 4**, classified as 3e.

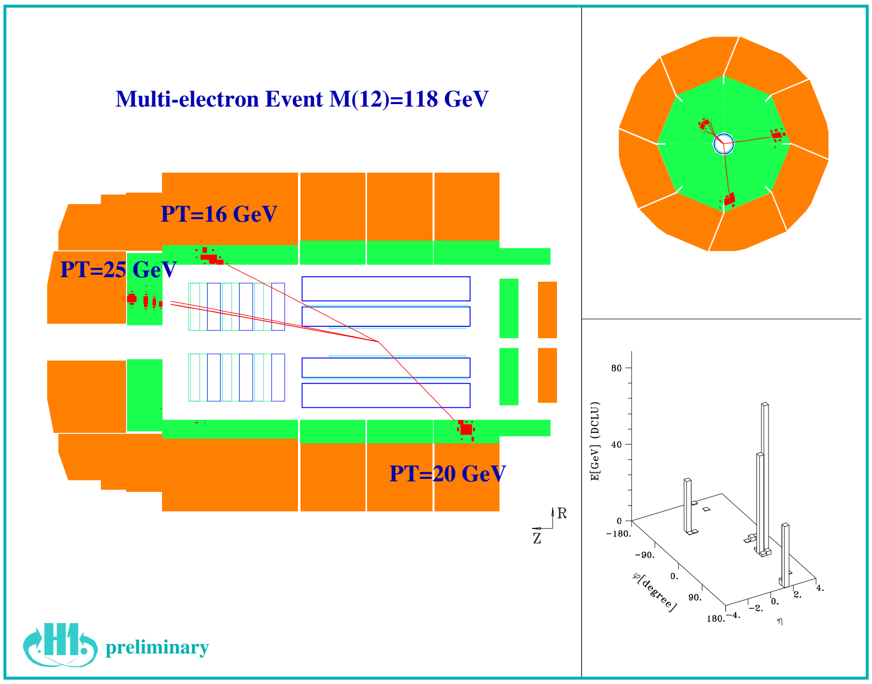

Figure 14: Event Display of **Event 5**, classified as 3e.

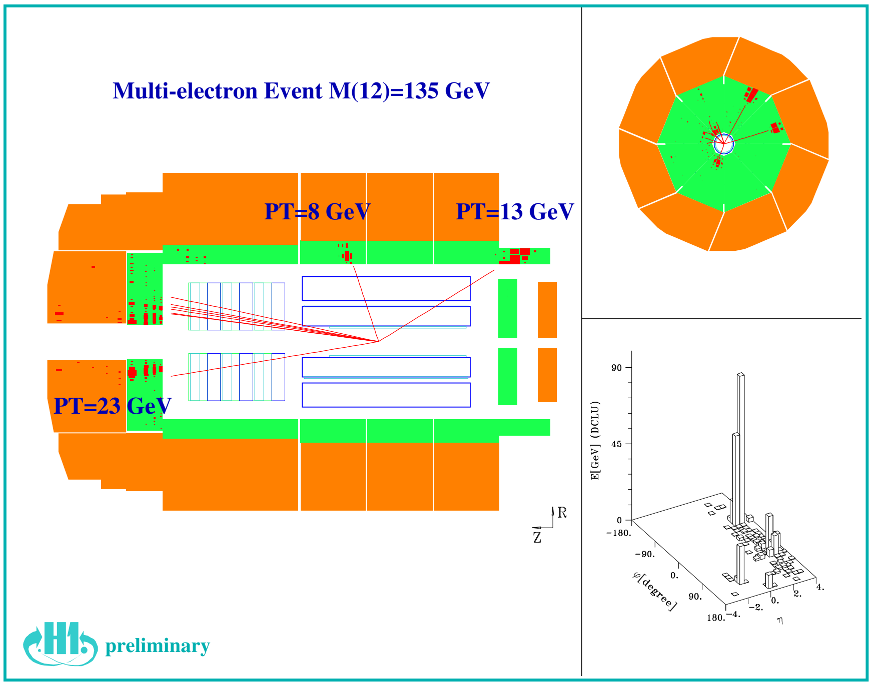

Figure 15: Event Display of **Event 6**, classified as 3e.

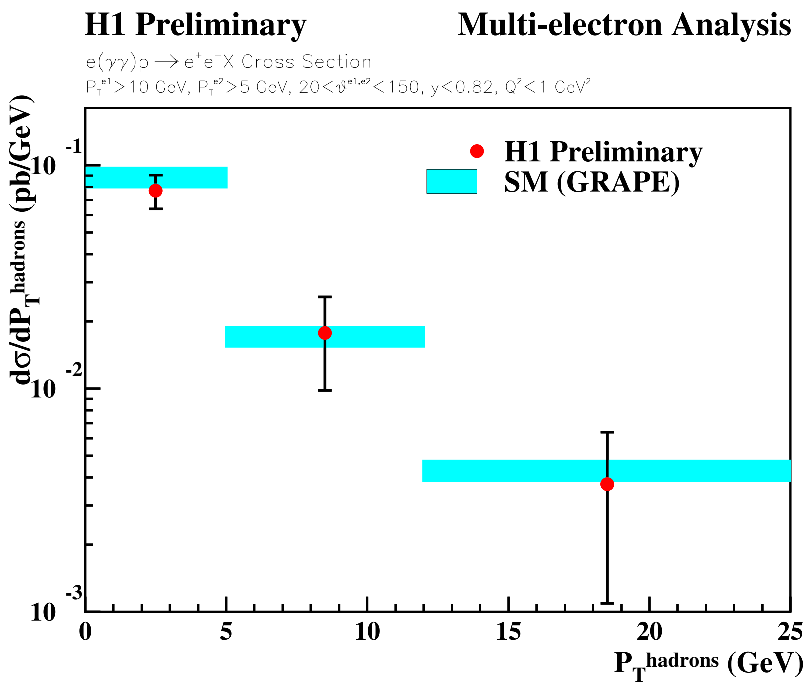

Figure 16: Cross section measurement of the photon-photon process as a function of the hadronic transverse momentum, compared to the Standard Model prediction.

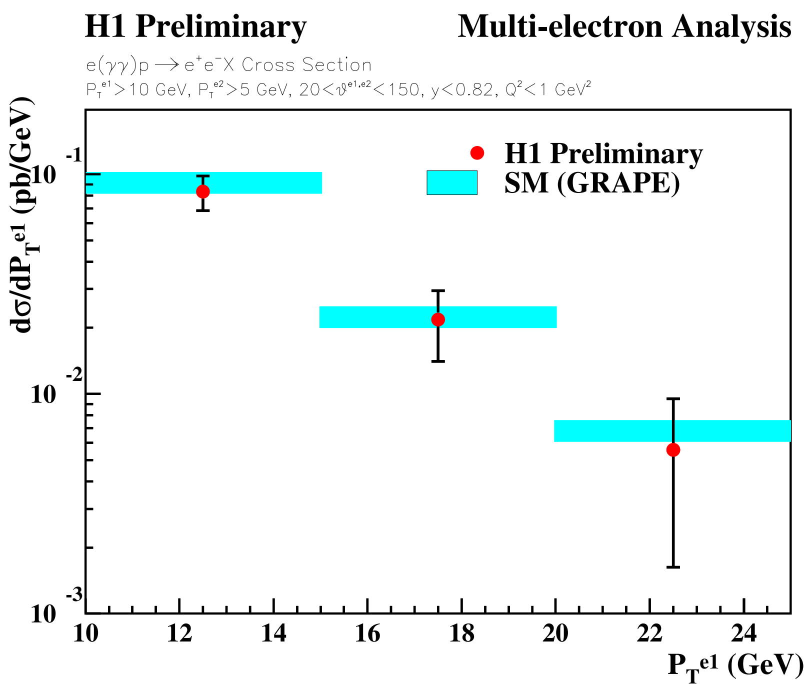

Figure 17: Cross section measurement of the photon-photon process as a function of the highest electron transverse momentum, compared to the Standard Model prediction.

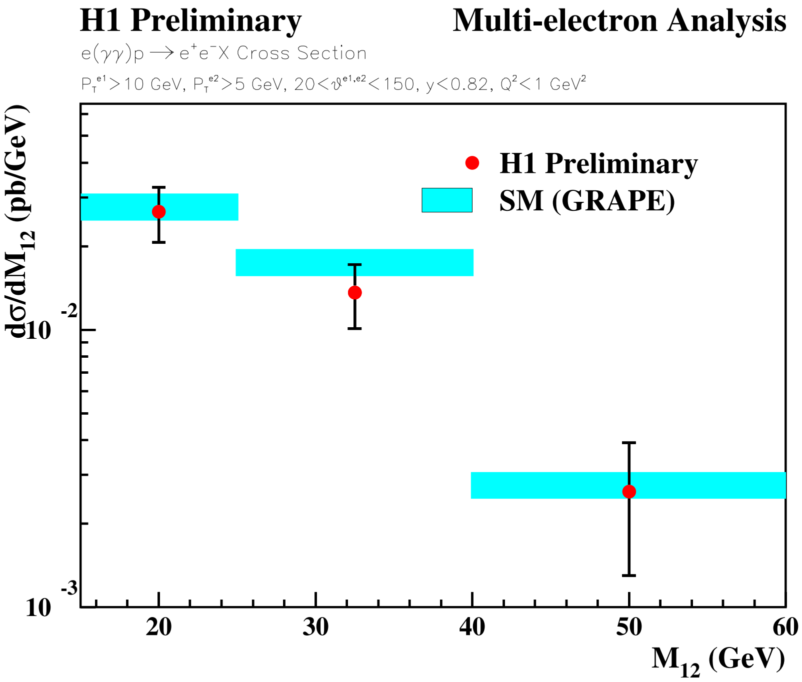

Figure 18: Cross section measurement of the photon-photon process as a function of the invariant mass of the highest-P_T electron pair, compared to the Standard Model prediction.